NMR Study of the Interaction between Zn(II) Ligated Bleomycin and *Streptoalloteichus hindustanus* Bleomycin Resistance Protein†

Christophe Vanbelle,‡ Bernhard Brutscher,‡ Martin Blackledge,‡ Claudia Muhle-Goll,‡ Marie-Hélène Rémy,§ Jean-Michel Masson,§,|| and Dominique Marion‡,*

Institut de Biologie Structurale, Jean-Pierre Ebel C.N.R.S.-C.E.A.-U.J.F., 41 rue Jules Horowitz, 38027 Grenoble Cedex, France, Institut de Pharmacologie et de Biologie Structurale, UMR 5089, 205 Route de Narbonne, 31077 Toulouse Cedex, France, and Institut National des Sciences Appliquées, Complexe Scientifique de Rangueil, 31077 Toulouse Cedex, France

Received August 27, 2002; Revised Manuscript Received October 18, 2002

ABSTRACT: Bleomycin (Bm), a 1.4 kDa glycopeptide excreted by *Streptomyces verticillus*, is a natural antibacterial compound used in therapy as antineoplastic drug. To counteract its biological activity, cells have developed several resistance mechanisms, one of these based on proteins able to tightly bind Bm. In this paper, the interaction of Zn^{2+}−Bm with the *Streptoalloteichus hindustanus* Bm resistance protein (ShBle) has been investigated by solution state NMR. Sequential nOe and chemical shift index have shown that the fold of the protein (in absence or presence of Bm) is identical to the previously published X-ray structure. The dimeric nature of ShBle is confirmed by the diffusion tensor as determined by NMR relaxation data. Using isotope filtered nOe experiment, intermolecular nOes between Bm and ShBle have been observed as used for modeling. While the interaction of the Bm metal binding site with ShBle appears to be uniquely defined, several conformations of the bithiazole moieties are compatible with the NMR data. Binding of Bm also induces changes of the local dynamics (stretch N85-G91), as shown by ^{15}N relaxation data. These results are discussed in the context of several Bm analogues able to interact with ShBle and of the recently published X-rays structures.

Bleomycin (Bm)[1] is a glycopeptide of molecular weight close to 1.4 kDa produced and excreted by a filamentous bacterium belonging to the actinomycetes family, *Streptomyces verticillus* (*1*). Whereas Bm is naturally used as an antibiotic in its native organism, it has excited interest since its discovery due to its potential chemotherapeutic application (*2*, *3*). Bleomycin is a potent antineoplastic drug which has been used for the past 30 years against testicular carcinoma, malignant lymphomas, and some squamous cell carcinomas without significant bone marrow toxicity. Unfortunately, Bm produces lung intersticial fibrosis and parenchymal injury. This dose-dependent, cumulative and irreversible side effect seriously hinders its clinical use. Bm anaerobically ligates a ferrous ion in a readily oxidizable form and, in the presence of molecular oxygen, cleaves double stranded DNA (*4*, *5*). In addition to Fe(II), Bm can bind to a number of other metals, e.g., Co(II), Co(III), Zn(II), Cu(II), and Cd(III) (*6*−*8*). The geometry of the Bm−metal ion complex has been shown to be octohedral, either penta- or hexa-coordinated, with six Bm ligands or five Bm and one water molecule ligands (Figure 1). A number of related molecules, differing from Bm by chemical modifications, have been reported, such as tallysomycin and phleomycin (*9*) (Figure 1, Supporting Information).

Prior to its use as an anticancer drug, Bm and analogues were identified as potent antibacterial compounds produced by actinomycetes to kill various types of organisms (prokaryotic as well as eukaryotic cells). Various Bm resistance determinants have been identified and characterized in prokaryots and eukariots. To counteract this antibiotic activity, attacked cells have designed several mechanisms of resistance, of which the most common involves the chemical modification of the Bm molecule, which can be *N*-acetylated (*10*) or deaminated by Bm hydrolases (*11*): in either case, the resulting compound lacks any antineoplasic activity. The producing bacteria also require protection from the lethal effects of Bm but cannot use irreversible modification to prevent function. Resistance determinant developed by bacteria involves a 14kDa Bm binding protein as isolated in *Streptoalloteichus hindustanus* (ShBle), *Streptomyces verticillus* (BLMA), and *E. coli* transposon 5 (BLMT) (*12*−*14*). The structures of these three Bm resistance proteins (BRP) as free form have been solved using X-rays crystallography (*15*−*17*) and are nearly superimposable. These proteins involved in the resistance mechanism by temporary drug sequestering are coded either by plasmid genes (Sa *ble* of *S. aureus* (*18*)) or by chromosomal genes (Sh *ble* of *S. hindustanus*).

† C.V. acknowledges the receipt of a Ph.D. fellowship from the French ministry of research and technology. C.M.-G. was supported by an EMBO postdoctoral fellowship.

* To whom correspondence should be addressed. Fax: + 33 438 78 54 94. E-mail: marion@ibs.fr.

‡ Institut de Biologie Structurale.

§ Institut de Pharmacologie et de Biologie Structurale.

|| Institut National des Sciences Appliquées.

[1] Abbreviations: Bm, bleomycin; Me−Bm, metal-bound bleomycin; ShBle, *Streptoalloteichus hindustanus* Bm resistance protein; BLMT, *E. coli* transposon 5 Bm resistance protein; BLMA, *Streptomyces verticillus* Bm resistance protein; f-ShBle, free ShBle; Zn−Bm−ShBle, Zn(II)−Bm−bound ShBle; Fe−Bm−ShBle, Fe(II)−Bm−bound ShBle; BRP, Bm resistance protein; CSA, chemical shift anisotropy; MES, morpholinoethansulfonic acid; nOe, nuclear Overhauser effect; NMR, nuclear magnetic resonance; R_1, $R_{1\rho}$, longitudinal and rotating frame relaxation rates; ESI-MS, electrospray ionization mass spectroscopy.

10.1021/bi0267341 CCC: $25.00
Published on Web 01/01/2003

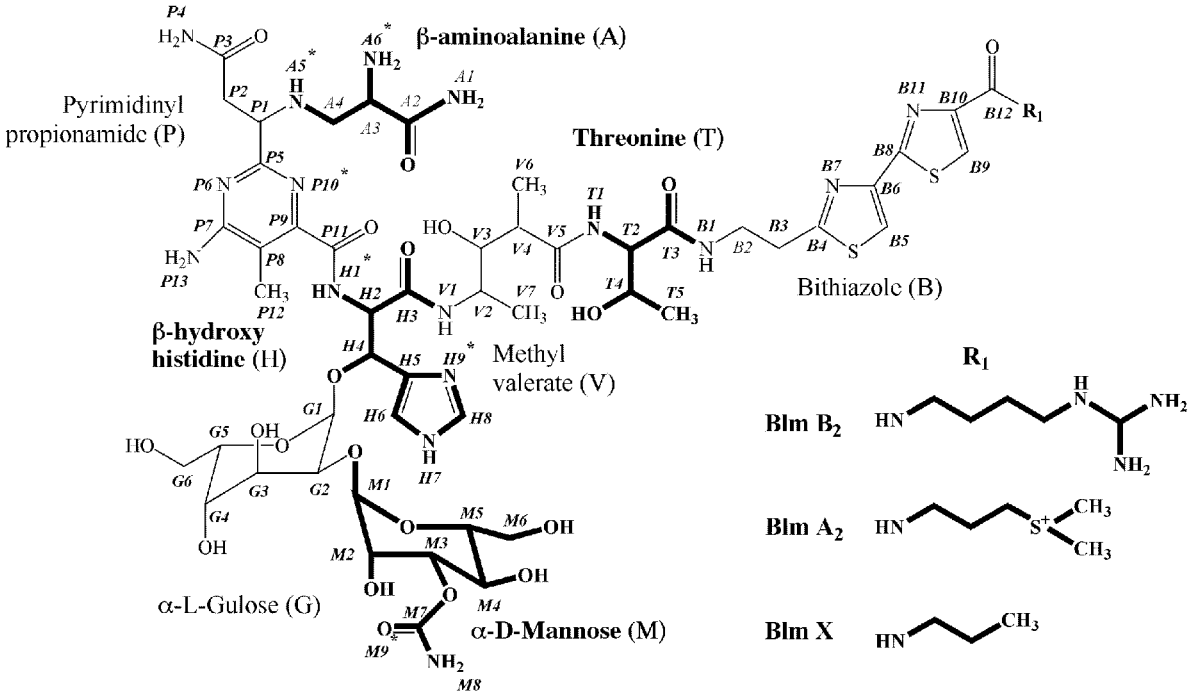

FIGURE 1: Chemical structure of bleomycins. The atoms numbering correspond to the used nomenclature. The metal ligand are notified with a star according to the Co(II)−Bm structure (*42*). Nitrogen P10, H1, H9, and A5 are the planar metal ligands.

These small proteins (containing about 124 residues) bind reversibly to Bm (*19*), thus preventing DNA cleavage. Intact Bm is then available to be released into the external medium when needed, although the mechanism of this release remains unknown. This drug sequestering, for efficient excretion to the environment, represents an optimized strategy for self-preservation of the drug-producing organism. In the case of another antitumor agent, mitomycin, from *Streptomyces lavendulae*, the gene corresponding to a membrane carrier transport protein (*20*), has been recently identified next to the locus corresponding to a drug binding protein.

The structure of *S. hindustanus* Bm resistance protein solved by X-rays crystallography (*15*) shows a homo-dimeric organization stabilized by an exchanged β strand and a hydrophobic interface. Each monomer comprises a structure in two halves with remarkable similarity of fold (α/β) despite negligible sequence similarity. In their study the authors also propose a structural model of the Cu(II)−Bm−ShBle complex, in which one ShBle dimer binds two Bm molecules, based on the individual crystal structures of the interacting molecules, and electrostatic and steric considerations. The proposed modes of binding of the Bm to DNA and to ShBle were compared and important interaction mechanisms identified. In particular, the authors suggest that the geometry of the antibiotic could be refined to allow differential DNA/protein binding. During our study, the crystal structures of the metal free Bm−BLMT (*17*) and the Co(II)−Bm−BLMA (*21*) complexes have been published. These structures confirm the interaction mode proposed in the previous models (*15*, *16*).

It has been shown on animal models that transgenic expression of BRP in mice (*22*) or adenovirus-mediated transfer of the BRP gene prevents bleomycin-induced pulmonary fibrosis (*23*). Characterization of the precise modes of protein/antibiotic binding is thus important for a better understanding of the basis of BRP activity that could lead to the development of other pharmaceutical products designed to enhance the chemotherapeutic efficiency of Bm analogues by decreasing their deleterious side effects. We have therefore initiated a detailed study of the structure and dynamics of the Zn−Bm−ShBle complex in solution.

The Zn^{2+} ligated form of Bm was chosen for the NMR study because of the diamagnetic properties of the Zn^{2+} ion. Complete resonance assignment of ShBle in the complex has been obtained as reported elsewhere (*24*), as well a partial assignment of the Bm ^{1}H resonances. In this study chemical shift mapping and changes in hydrogen−deuterium exchange rates were used to identify the binding interface. ^{15}N relaxation measurements have been used to monitor changes in intramolecular dynamics on a pico- to millisecond time scale. The dimeric architecture of ShBle in the complex was also analyzed using the hydrodynamic properties of the molecule derived from ^{15}N relaxation data. Finally, an experimental model of the Zn−Bm−ShBle complex has been calculated on the basis of a set of intermolecular ^{1}H-^{1}H nOes.

MATERIALS AND METHODS

ShBle Expression and Purification. The *Sh ble* gene coding for ShBle was cloned from the plasmid pUT 50 (generous gift of Pr. Tiraby) between the Nco I and Hind III restriction sites of the pET-26b(+) (Novagen), by PCR using the respective oligonucleotides Sh1 CCATGGCCAAGTTGACCAGTGCCGTTGGGGTGCTCACC and Sh2 AAGCTTATCAGTCCTGCTCCTCGGCCAC as primers. The obtained plasmid will be referred as pSh, where the underlined sequences are the target of the restriction enzyme. The *E. coli* expression strain HMS 174 (DE3) is transformed with pSh. This system leads to the periplasmic expression of the ShBle, according to the sequence referenced as P17493 in the Swiss-Prot database and shown in Figure 3. Uniformly ^{15}N and ^{13}C/^{15}N-labeled ShBle was obtained by growing *E. coli* in minimal M9 media (*25*) containing 1 g/L $^{15}NH_4Cl$

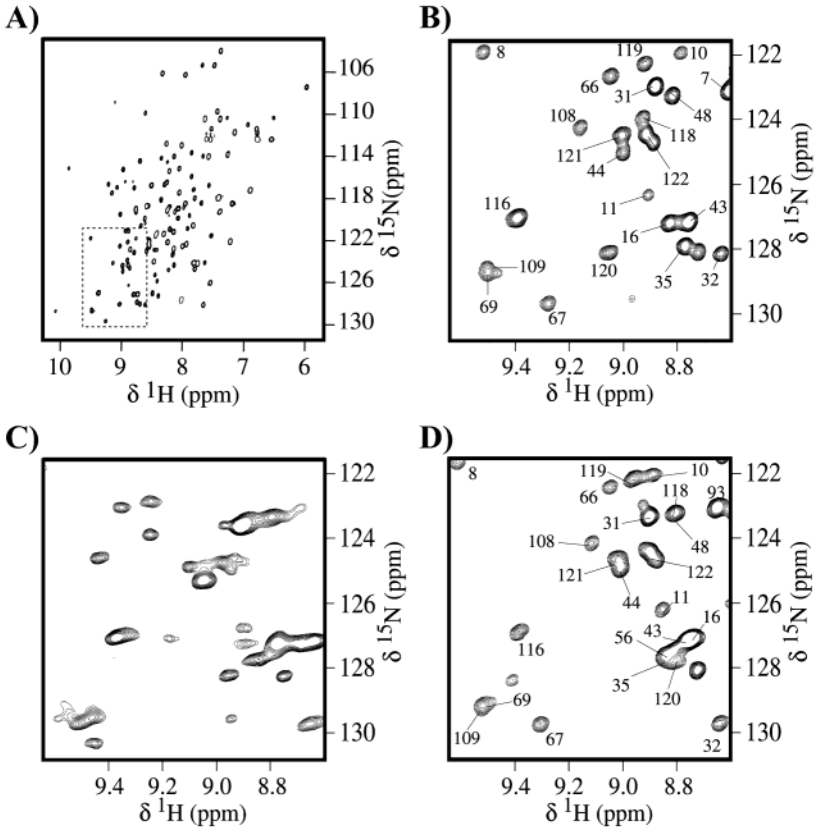

FIGURE 2: ^{1}H-^{15}N HSQC correlation spectra of (A, B) f-ShBle, (C) Fe(II)−Bm-bound, and (D) Zn−Bm−ShBle. For better comparison, only a small part of the spectrum is plotted in inserts (B−D).

and 2 g/L [$^{13}C_6$]-glucose, and 50 μg/mL kanamycin. ^{15}N labeled NH_4Cl and ^{13}C labeled glucose were purchased from Martek and Cambridge Isotopes, respectively. The cells were grown in a shaker at 30 °C until the OD^{600} reached about 0.6, and then the protein expression was induced by adding 0.1 mM IPTG. The cells were harvested 16 h later.

ShBle purification begins by the periplasmic protein recovery, obtained by applying an osmotic shock to the pellet, as described in the Novagen's pET system manual. The periplasmic extract was adjusted at pH 5 with 0.5M piperazine buffer and loaded on a 2.5 × 10 cm Q Sepharose Fast Flow column equilibrated with a 20 mM piperazine buffer pH 5 (buffer A) at 5.3 mL/min flow rate. Elution was performed with a NaCl step gradient. The fractions (0.3M NaCl) containing ShBle were combined. The solution was dialyzed against buffer A and loaded into a MonoQ HR 5/5 equilibrated with buffer A. The protein was then eluted with 20 mL linear gradient of 0.15−0.5M NaCl in buffer A at 0.5 mL/min. Each fraction was analyzed by gel filtration on Superose 12HR (10/30). The fractions containing ShBle were pooled and concentrated. All chromatographic media were purchased from Pharmacia Biotech. This leads to ShBle at high homogeneity, as measured from PAGE-SDS gel, whereas the ESI-MS molecular weight measurement reveals two species in a 0.7:0.3 ratio (*50*). The major species corresponds to the expected sequence. The minor species fits with a misprocessing of the periplasmic addressing peptide, leading to an extra A−M−A sequence. This feature may explain the two correlation peaks detected for the Ala-2 and Lys-3 residues in the ^{1}H-^{15}N HSQC spectrum, with a similar intensity. This ShBle was used without further purification.

Bleomycin Characterization. Bm was obtained as a gift from Rhône Poulenc (Paris, France). The ES mass spectrometry reveals a mixture of three compounds (1351.6/1413.4/1424.6 Da) with a 1:1:1 ratio (*50*). Bm was previously reported as a mixture of two components Bm A2 (1413.4 Da) and B2 (1424.6 Da) in 2:1 ratio (*26*), which differ at the terminal amide (R_1 in Figure 1). The 1351.6 Da form (Bm X) probably arises from Bm A2 through an undetermined chemical modification and could correspond to a linear aliphatic chain (R_1: $CH_2CH_2CH_3$). The Bm mixture was used for our study without any further purification as no evidence was found for differential binding of the three forms (see below).

NMR Sample Preparation. NMR samples (450 μL) were prepared in 20 mM deuterated MES (from A. R. C. Isotopes) pH 6.5 buffer in 10% D_2O or 99% D_2O, supplemented with 100 mM NaCl, and 0.02% sodium azide. The complex formation between ShBle and metal−bleomycin was monitored using a ^{15}N labeled protein sample at 200 μM concentration. Two ternary complexes were studied: Zn−Bm−ShBle and Fe−Bm−ShBle. Both metals were introduced as sulfate salts (Fluka). Bm was first mixed with $ZnSO_4$ ($FeSO_4$ receptively) in a 1:1.2 ratio to form a Bm−metal complex, which was then added to the native ShBle in a 1:1 ShBle:Bm ratio to form the ternary Zn−Bm−ShBle (Fe−Bm−ShBle) complex. Due to the extreme sensitivity of Fe(II)−Bm to oxidation, the Fe−Bm−ShBle complex was prepared in gloves box under strict oxygen-free conditions. For this reason, 5 mM dithionite is added to the Fe(II) samples. An easy way to track the reductive state of the Fe(II)−Bm complex is its specific pink color due to its absorbance maxima at 480 and 370 nm (*4*). For both f-ShBle

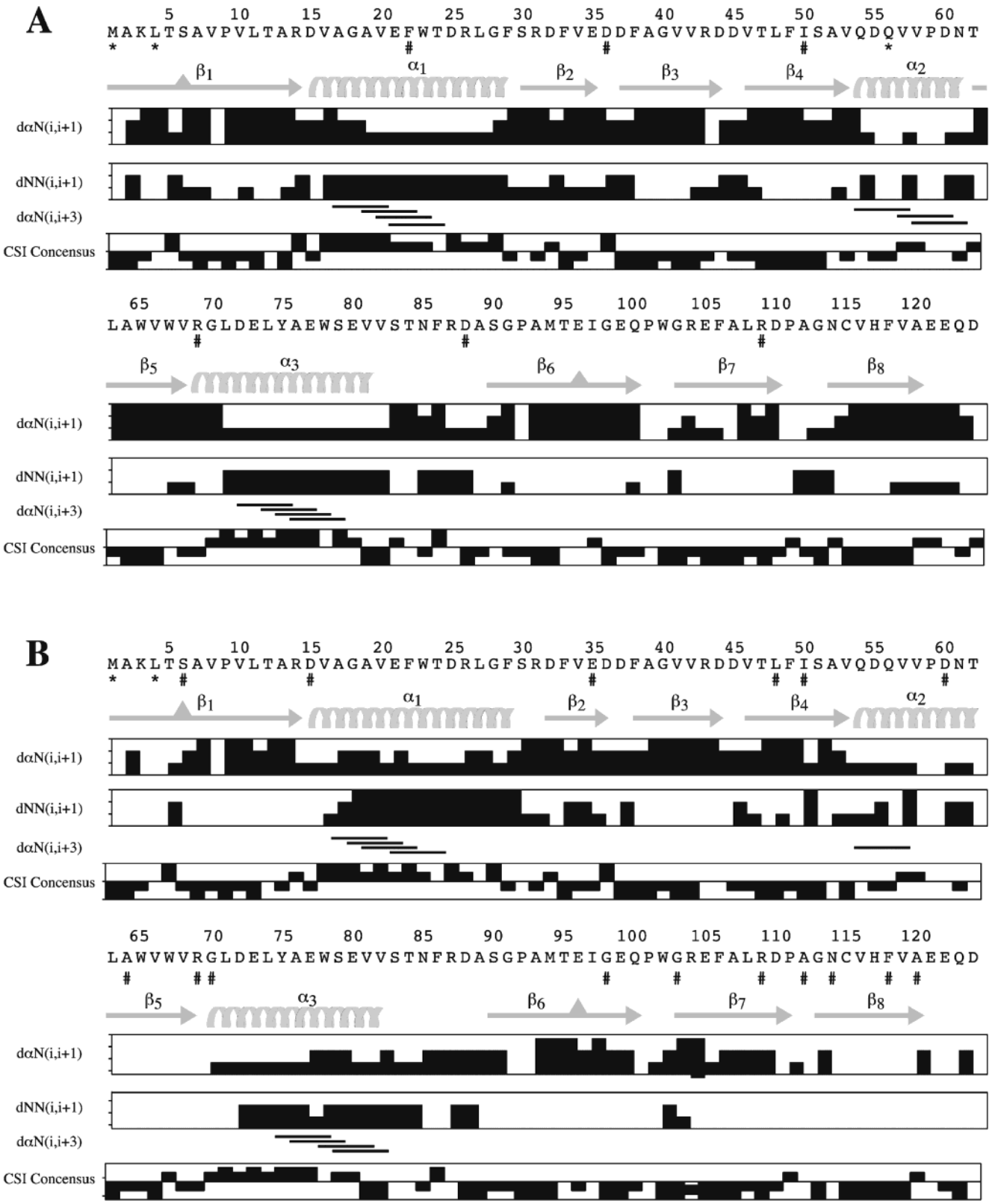

FIGURE 3: ^{1}H-^{1}H nOe and CSI data observed for (A) f-ShBle and (B) Zn−Bm−ShBle. The identified secondary structural elements for both forms are indicated by arrows (β-strand) and helices (α-helix). A filled triangle on an arrow stands for an irregularity of the canonical β-strand structure. $*$ indicates not-assigned HSQC peaks, and # corresponds to residues with overlapping ^{1}H-^{15}N HSQC correlation peaks. Slowly exchanging amide proton are indicated by bold italic case.

and Zn−Bm−ShBle, resonance assignment was achieved on a 1 mM ^{13}C/^{15}N labeled sample (24) and ^{15}N relaxation studies were performed on a 1 mM ^{15}N labeled sample. For resonance assignment of Bm in the Zn−Bm−ShBle complex and for the intermolecular NOESY experiments two 1 mM ^{13}C/^{15}N labeled samples were used: one in 10% D_2O/ 90% H_2O and another in 99% D_2O. For the latter, the 450 μL protein sample was extensively dialyzed against the final

buffer in a 1 mL slide-Dyalyser (Pierce 5 kDa cutoff) and lyophilized three times in D_2O. The Bm−metal complex was added before lyophilization.

NMR Spectroscopy and Data Analysis. All NMR experiments were performed on Varian INOVA 600 or INOVA 800 spectrometers, both equipped with a triple-resonance (^{1}H, ^{15}N, ^{13}C) probe and shielded *z*-gradients. Unless otherwise stated, the sample temperature was set to 40 °C. NMR experiments used for ShBle backbone and side-chain resonance assignment have been described previously (*24*). Data processing and peak picking were performed using FELIX program version 97.0 (MSI Technologies).

^{15}N Relaxation Measurements. ^{15}N R_1 and $R_{1\rho}$ relaxation rate and {^{1}H}-^{15}N nOe measurements were carried out on a ^{15}N labeled sample at 600 MHz ^{1}H frequency as described elsewhere (*27*, *28*). The {^{1}H}-^{15}N nOe can be used as a measure of the amount of local motion in the picosecond to nanosecond time range. The ^{15}N transverse relaxation rates ($R_{1\rho}$) contain a contribution from conformational exchange on a μs to ms time scale, but they are also sensitive to fast time scale fluctuations. To discriminate the two contributions, we have measured an additional relaxation rate $\Gamma_{N,NH}^{CSA,DD}$, which is due to a cross correlation effect between the ^{15}N-^{1}H dipolar interaction and the ^{15}N chemical shift anisotropy (CSA). $\Gamma_{N,NH}^{CSA,DD}$ is insensitive to conformational exchange, while having a similar dependence on rotational diffusion and internal fast-time scale motion as $R_{1\rho}$ (*29*). The ratio $\rho = R_{1\rho}/\Gamma_{N,NH}^{CSA,DD}$ is used to monitor local backbone motion on the μs to ms time scale.

R_1 and $R_{1\rho}$ values were obtained by fitting the measured peak heights to a two parameter function described as $I(T) = I_0 \exp(-RT)$, where $I(T)$ is the intensity after a delay time T and I_0 is the intensity at $T = 0$. The steady-state heteronuclear nOe values were determined from the ratios of the measured peak intensities in the presence (I_{sat}) and absence (I_{ref}) of ^{1}H saturation as $NOE = I_{sat}/I_{ref}$. Additional cross-correlated relaxation rate constants $\Gamma_{N,NH}^{CSA,DD}$ were measured using a constant time (CT) TROSY-type ^{1}H-^{15}N correlation experiment (*30*, 31), where the two ^{15}N doublet components are separated in two spectra. The $\Gamma_{N,NH}^{CSA,DD}$ values are obtained from a one-parameter fit to the function $I^{\alpha}(T)/I^{\beta}(T) = \exp(\Gamma_{N,NH}^{CSA,DD}T)$, where $I^{\alpha}(T)$ and $I^{\beta}(T)$ are the peak heights measured in the doublet-separated TROSY spectra. Special care was taken to ensure a constant sample temperature among the different relaxation experiments by applying off-resonance heat compensation RF pulses during the recycle delays (*32*). The recycle delay was set to 2.5s for R_1, $R_{1\rho}$, and $\Gamma_{N,NH}^{CSA,DD}$ and to 7 s for the heteronuclear nOe measurements. The exponential relaxation decay was sampled at the following time points: R_1: 15, 90, 240, 390, 540, 690, and 990 ms; $R_{1\rho}$: 8, 16, 32, 48, 64, 104, and 132 ms; and $\Gamma_{N,NH}^{CSA,DD}$: 20, 40, 60, 80, and 100 ms. The first time point of each measurement series is repeated at the end to assess the time stability of the measurement and evaluate possible systematic errors. For $R_{1\rho}$ measurements, a ^{15}N spin-lock field was applied during the transverse relaxation period with a strength of $|\gamma_N B_1|/2\pi = 2.5$ kHz. The measured $R_{1\rho}$ values were corrected for resonance offset effects using the equation

$$R_{1\rho}^{Corr} = (R_{1\rho}^{Meas} - R_1 \sin^2\theta) \text{ with } \theta = \tan^{-1}\left(\frac{\Delta\upsilon_N}{\gamma_N B_1}\right)$$

and $\Delta\nu_N$ the frequency difference between the ^{15}N carrier and the frequency of the observed nitrogen.

Determination of Molecular Tumbling Diffusion Tensor. The relaxation data measured for individual amide ^{15}N have been analyzed in terms of a single spectral density function $J(\omega)$, reflecting the random fluctuations of the N−H vector. In the model-free approach of Lipari-Szabo (*33*) $J(\omega)$ splits into two terms taking into account the overall molecular tumbling and intramolecular fluctuations, respectively. For the general case of anisotropic molecular tumbling the measured relaxation rates depend on the orientation of the N−H vector with respect to the diffusion tensor (**D**) as described by Woessner (*34*). The orientation and principal axes values of **D** were obtained by selecting a subset of residues involved in regular secondary structural elements, and exhibiting only small-amplitude internal motion (as measured from the heteronuclear nOe) and minimizing the target function

$$\chi^2 = \sum_n \left(\left(\frac{R_{1\rho}^{meas}}{R_1^{meas}} - \frac{R_{1\rho}^{calc}(D)}{R_1^{calc}(D)} \right) / \sigma_n^2 \right)$$

where σ is the uncertainty in the experimental $R_{1\rho}^{meas}/R_1^{meas}$ ratio. The sum is performed over all N−H groups in the selected experimental data set. The fit of the diffusion tensor components and orientation is performed using the program TENSOR2, a simulated annealing-based algorithm developed in our laboratory (*35*). TENSOR2 calculates the molecular diffusion tensor on the bases of a list of measured R_1 and $R_{1\rho}$ rate constants and the coordinates of the molecular structure. TENSOR2 also performs Monte Carlo simulations to evaluate the uncertainty of the fitted diffusion parameters and to test the statistical significance of the resulting models.

Deuterium−Hydrogen Exchange Measurements. Deuterium−hydrogen exchange rates depend on solvent accessibility of the exchangeable protons, and thus the 3D structure and conformational flexibility of the protein (see, for example, ref *36*). To probe the amide proton exchange rates along the protein backbone, we have recorded ^{1}H-^{15}N HSQC spectra on f-ShBle and the Zn−Bm−ShBle complex after one month of incubation in 99% D_2O at 20 °C.

Isotope-Edited/Filtered ^{1}H-^{1}H TOCSY and ^{1}H-^{1}H NOESY Experiments. For ^{1}H resonance assignment of Bm in the Zn−Bm−ShBle complex, two-dimensional ^{1}H-^{1}H TOCSY and ^{1}H-^{1}H NOESY spectra were recorded at ^{1}H = 800 MHz on the ^{13}C/^{15}N-labeled Zn−Bm−ShBle complex dissolved in either 10% or 99% D_2O. The pulse sequences include double-tuned ^{13}C/^{15}N isotope filters (*37*) before and after the TOCSY or NOESY mixing to suppress correlation peaks originating from ShBle and, in the case of NOESY, between ShBle and Bm. No heteronuclear decoupling was applied during ^{1}H frequency labeling in t_1 and t_2 to identify residual signals from ShBle not removed by the filter, which then appear as a doublet. Experiments performed on a sample dissolved in H_2O used an additional WATERGATE sequence prior to detection for water suppression (*38*). The NOESY mixing time was set to 100 ms. For TOCSY mixing, two spectra were recorded using DIPSI-2 composite pulse trains with overall duration of 20 and 60 ms, respectively. The total acquisition time for 300 × 512 complex data points was 15 h per experiment.

Intermolecular nOe between Bm and ShBle were observed in a three-dimensional ^{13}C edited ^{1}H-^{1}H NOESY spectrum by inserting an additional double-tuned ^{13}C half filter (*39*) prior to the NOESY mixing (100 ms mixing time). To limit the relaxation delays, no ^{15}N filter was applied as the experiment was performed in D_2O, and only a few nOe's were expected between the slowly exchangeable amide protons of ShBle and Bm. 110(^{1}H) × 54(^{13}C) × 512(^{1}H) complex data points were recorded for spectral widths of 8000 Hz (^{1}H), 12500 Hz (^{13}C), and 10400 Hz (^{1}H) in an experimental time of 64 h. To enhance the sensitivity, a two-dimensional experiment including the double-tuned ^{13}C half filters without edition of the ^{13}C frequency was also recorded.

Chemical Shift Mapping of Bm Binding. Protein-binding surfaces can be mapped by observing the changes in chemical shift between the free and the bound states of the protein (*40*, *41*). As mentioned previously, the Bm−ShBle complex is in slow exchange, as compared to the NMR time scale. With assignment of both forms, the weighted chemical shift variation $\Delta\delta$ was calculated according to

$$\Delta\delta = 6.7|\Delta\delta_H| + |\Delta\delta_N| + 1.1|\Delta\delta_{C\alpha}| + 2.5|\Delta\delta_{C'}| - \sqrt{2(6.7\phi_H^2 + \phi_N^2 + 1.1\phi_{C\alpha}^2 + 2.5\phi_{C'}^2)}$$

where $\Delta\delta_H$, $\Delta\delta_N$, $\Delta\delta_{C\alpha}$, and $\Delta\delta_{C'}$ are the $^{1}H^{N}$, $^{15}N^{H}$, $^{13}C^{\alpha}$, and $^{13}C'$ chemical shift differences between f-ShBle and Zn−Bm−ShBle in parts per million, respectively, and ϕ_N, ϕ_H, $\phi_{C\alpha}$, and $\phi_{C'}$ correspond to the digital resolution to which the frequency can be measured in the 3D NMR spectra (ϕ_N = 0.1 ppm, ϕ_H = 0.1 ppm, $\phi_{C\alpha}$ = 0.4 ppm, $\phi_{C'}$ = 0.1 ppm). The weighting factors of the individual terms normalize the chemical shift range for each nucleus. The above equation amounts to considering only changes larger than a threshold defined by the digital resolution. Should a nucleus not be assigned in either of the two forms, then the corresponding term is dropped from the above expression.

Restrained Molecular Dynamics of Zn−Bm−ShBle Complex. To characterize the protein−antibiotic interaction, we have performed restrained molecular dynamics simulations using two different sets of constraints. Set 1 (**S^{1}**) contains the experimentally observed distances between Zn−Bm and ShBle (30 constraints) as well as 23 intramolecular Bm distances derived from the three-dimensional ^{13}C edited ^{1}H-^{1}H NOESY and two-dimensional double filtered ^{1}H-^{1}H NOESY spectra, respectively (Tables 1 and 2 in Supporting Information). Set 2 (**S^{2}**) contains the distances present in **S^{1}** and additional nonexperimental distances between the bithiazole fragment and ShBle (Table 3 in Supporting Information). These additional distances between the bithiazole tail and ShBle were obtained from the modeled Bm−ShBle complex with the aim of testing the compatibility of our NMR data with the previously proposed model.

Calculations were performed using the Discover Version 2.98 molecular dynamics program (MSI Technologies), with the AMBER4 force field, modified to incorporate parameters characterizing Fe−BmA_2, used to mimic the Zn−Bm complex. The metal coordination sphere was derived from the Co(II)−Bm NMR structure (PDB code 1DEY) (*42*) using InsightII (MSI Technologies). The X-rays structure of f-ShBle (*15*) is used as template for the simulation (PDB entry 1BYL). Protons were added to the coordinates, and the structure was then energy-minimized with the heavy atoms fixed. All nOe interactions were treated as ambiguous constraints between protons present in either subunit of the dimer and the antibiotic. The initial position of the two molecules was chosen to allow apparently direct access of the antibiotic to the most probable interaction site as determined from NMR chemical shift mapping, hydrogen exchange measurements, and the observed intermolecular ^{1}H-^{1}H nOe. 31 and 13 structures were calculated for **S^{1}** and **S^{2}**, respectively, using the following protocol.

The system was equilibrated at 500 K for 5 ps using direct velocity scaling, followed by a 5 ps sampling period during which the structure of the Zn−Bm was free to sample conformational space, thereby varying the initial relative orientation of the interacting molecules. During this period the ShBle was fixed to the crystallographic coordinates. The ShBle was then released, and for the remainder of each calculation only the backbone atoms of the protein were tethered to their initial positions by incorporating the additional energy term

$$E_{teth} = K\sum_i \sqrt{(x_i - x_i^0)^2/N}$$

into the potential energy function. x_i's are the Cartesian coordinates of the atoms to be tethered and x_i^0's the target coordinates. A force constant of K_{teth} = 500.0 kcal mol^{-1} Å^{-1} was used to restrain the N = 984 atoms to the coordinates of the crystal structure and side chains were free during the calculation. Simultaneously, the ambiguous restraints representing experimentally determined intermolecular contacts were gradually introduced into the calculation. Following minimization using steepest descent and conjugate gradient algorithms with a distance force constant K_{dist} of 5.10^{-4} kcal mol^{-1} Å^{-2} and 5 ps of equilibration at 500 K, the antibiotic was directed toward the active site during sampling periods of 2 ps. After each period the distance force constant was multiplied by a factor 10 until K_{dist} = 50 kcal mol^{-1} Å^{-2}, at which point the system was allowed to evolve, still at 500 K during a further 10 ps. The system was then slowly cooled to 100 K over a period of 10 ps. This was followed by energy minimization in the same force field. Nonbonded interactions were ignored beyond 10 Å and a switching function applied from 8.5 to 10 Å. A time step of 1 fs was used for all molecular dynamics simulations. No electrostatic terms were used. The calculation was repeated using different initial velocity distributions and relative starting positions as described.

Structures with the lowest experimental nOe violation energy were selected for final analysis. The interaction surface is measured on the basis of the accessible surface of the different partners implicated or not in the complex, using the GRASP program (*43*).

RESULTS

Evidence of Complex Formation between Me−Bm and ShBle. The formation of the binary Me−Bm complex was monitored by one-dimensional (1D) ^{1}H NMR. The Zn(II)− and Fe(II)−Bm spectra are similar to those obtained in previous NMR studies (*7*, *44*). The Me−Bm complex formation was independently confirmed by ESI-MS under nondenaturating conditions (*50*).

The formation of the ternary Me−Bm−ShBle complex was demonstrated by comparing ^{1}H-^{15}N HSQC spectra of ShBle in the absence of Bm (Figure 2A,B) and in the presence of Fe(II)−Bm (Figure 2C) or Zn(II)−Bm (Figure 2D). In both cases, a number of signals in the HSQC spectrum exhibit significant shifts compared to the free form; note that no shifts are observed (data not shown) when a metal is added to ShBle without Bm, a result which suggests a lack of direct interaction of these divalent ions with the protein. The spectral changes induced by the complex formation are however different for the two metals. In the case of Zn−Bm, all lines remain narrow and some of them move; the spectral changes for the Fe(II) complex are more dramatic, inducing broader lines and larger shifts. These differences can be mainly ascribed to the paramagnetic nature of the Fe(II) complex (*44*). As some valuable information may be obscured for nuclei close to the paramagnetic ion, we have decided to focus on the diamagnetic Zn−Bm−ShBle complex in our study. This complex is also easier to handle, without any special attention to oxygen in contrast to the Fe(II) complex where strict anaerobic conditions are mandatory.

At intermediate concentrations of Zn−Bm (data not shown), two ^{1}H-^{15}N correlation peaks are observed for most residues, indicating that the binding of Zn−Bm to ShBle is slow on the NMR time scale. No significant difference in binding of the three forms of Bm present in the mixture (A2, B2, and X) could be detected in our spectra. This implies that the variable part (R) of Bm is not directly involved in the interaction of Bm with ShBle.

Structural Characterization of f-ShBle and Zn−Bm−ShBle. Secondary Structural Elements. As the exchange between f-ShBle and Zn−Bm−ShBle is slow on the NMR time scale, the NMR resonance frequencies had to be assigned independently for the two forms and could not be simply inferred from exchange experiments. Almost complete backbone assignments for f-ShBle, as well as ^{1}H and ^{13}C of nonaromatic side chains for the Zn−Bm−ShBle complex were obtained (*24*).

The NMR information on the secondary structure elements in f-ShBle derived from sequential nOe (*45*) and the chemical shift index (CSI) (*46*) is summarized in Figure 3A. Eight β-strands and three α-helices can be identified, in general agreement with the crystal structure (*15*). A minor exception is the β_6 strand, which in the crystal structure begins at residue 92, while NMR data support a β-strand terminus already at residue 90. Furthermore, the missing negative CSI values for residues 95 and 96 indicate a deviation from a canonical structure at this position in the β_6 strand. A break of the hydrogen pairing with its partner strand (β_7) at this position has been observed in the crystal structures of ShBle (*15*) and BLMA (*16*). The same pattern in terms of secondary structure is seen for the Zn−Bm−ShBle (cf. Figure 3B). The interaction of ShBle with Zn−Bm does not induce any significant changes in the secondary structure of ShBle, as the same pattern of β-strands and α-helices is identified.

β-Sheet Topology. The β-sheet topology of ShBle was established from a set of long-range H^{α}-H^{N} nOe between the different β-strands detected in the ^{15}N-edited NOESY spectrum. The crystal structure of the f-ShBle shows a pseudosymmetry at the level of the monomeric secondary structures. A first half contains strands β_1, β_2, β_3, and β_4 as well as the α-helix α_1, whereas the second half includes strands β_5, β_6, β_7, and β_8 and helix α_3. These two moieties are linked together by a short helix α_2 (residues 54−61). The β-sheet topologies derived from the NMR data for f-ShBle and Zn−Bm−ShBle are in agreement with the crystal structure (Figure 4). As shown earlier on the basis of the CSI, the pairing of strands β_6 and β_7 is irregular and forms a bulge.

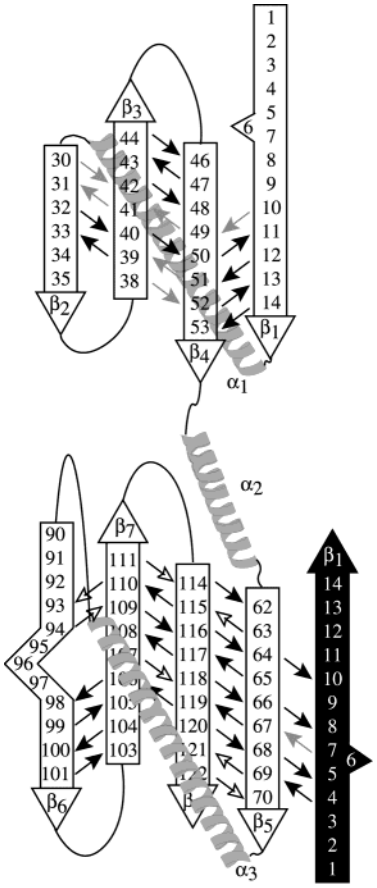

FIGURE 4: Topology of secondary structural elements as identified for f-ShBle and Zn−Bm−ShBle using long-range ^{1}H-^{1}H nOe (correlation peak between H^{i}_{α} and H^{j}_{N} in the 3D NOESY−HSQC spectrum). The arrows indicate nOe detected for both forms (plain black), f-ShBle only (grey), and the Zn−Bm−ShBle complex (empty).

f-ShBle is dimeric as shown by crystallography and ultracentrifugation studies. Intra- and intersubunit β-strand nOe's were differentiated by comparison with the crystal structure (*15*). The nOe observed in f-ShBle between residues 5 and 8 (β_1) with residues 66−69 (β_5) apparently correspond to intersubunit contacts, as a result of an arm exchange (Figure 4). These nOe remain unaffected in the Bm−ShBle form, providing evidence of the conservation of the quaternary structure on binding. Ultracentrifugation data are also in favor of a homodimer formation when Bm is bound (*15*).

Validation of the Dimeric Model from ^{15}N Relaxation Data. An independent confirmation of the dimeric nature of the protein is provided by the rotational diffusion tensor derived from ^{15}N relaxation data. The model-free formalism (*33*) provides a convenient way of separating internal flexibility and overall tumbling, assuming that they are not correlated.

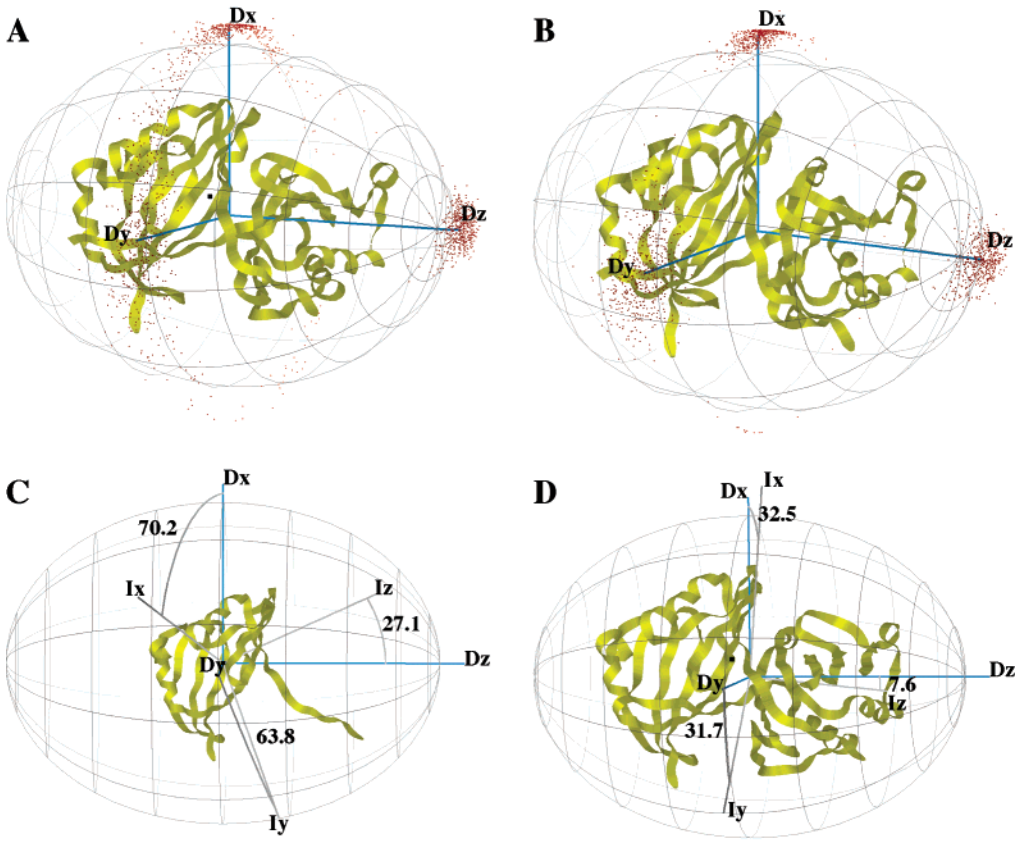

FIGURE 5: Rotational diffusion tensor ($\mathbf{D}_{xyz}$) determined on the basis of ^{15}N relaxation rate constants for (A) f-ShBle and (B) Zn−Bm−ShBle. The different points on the ellipsoid are the results of a Monte Carlo simulation ($n = 500$). In panels C and D the principal axes of the inertia (I_{xyz}) and diffusion tensors of f-ShBle are superimposed for monomeric and dimeric state, respectively.

The molecular diffusion tensor can be derived for a protein of known structure from a set of ^{15}N R_1 and $R_{1\rho}$ relaxation data measured for residues located in secondary structure elements. For these residues it can be safely assumed that spin relaxation is not affected by large-amplitude local motions. According to this criterion, a set of 54 nonoverlapping ^{15}N-^{1}H cross-peaks was chosen for f-ShBle and a set of 47 peaks for Zn−Bm−ShBle (Figure 1 in the Supporting Information). The optimization was carried out on a single monomer of the X-rays structure, i.e., the dimeric nature of ShBle is not provided as input information. The precision of the angular characterization of the diffusion tensor is illustrated graphically for f-ShBle (Figure 5A) and Zn−Bm−ShBle (Figure 5B): the dots surrounding the ellipsoid depict the results of the Monte Carlo (MC) simulation ($n = 500$). In both cases, the orientation of the D_{zz} component is rather well defined, but the two other components (D_{xx} and D_{yy}) are scattered around the circumference of an ellipse. This trend is more pronounced for the free form and is may be due to the lower quality of the experimental relaxation rates. Within the precision of our data, no significant difference is detected for the rotational diffusion of f-ShBle and Zn−Bm−ShBle.

We have compared the orientation of the principal axes of the diffusion tensor with the principal components of the inertia tensor (**I**), assuming either a monomeric or a dimeric form for f-ShBle. We can conclude that it is unlikely that the ShBle molecule exists in solution as a monomer, as the diffusion tensor does not correspond to the expected inertia tensor (Figure 5C). In the case of a symmetric homodimer, one of the axes of the diffusion tensor (as well as one of the axes of the inertia tensor) should coincide with the symmetry axis of the dimer. In Figure 5D, the axes of the inertia tensor of f-ShBle identify I_y as the symmetry axis. While our data do not permit the full characterization of the orientation of the diffusion tensor axis, it is of interest to note that the I_y falls in the plane defined by D_{xx} and D_{yy}, i.e., the plane orthogonal to the best defined axis D_{zz} of the diffusion tensor. The same comparison is performed for the Zn−Bm−ShBle. The dimer also leads to the best fit between the diffusion and the inertia tensors (I_xOD$_x$ = 78.6°/41.2°, I_yOD$_y$ = 73.7°/40.9°, and I_zOD$_z$ = 25.4°/10.8° for the monomeric and dimeric forms respectively considered).

Resonance Assignment and Structural Characterization of Bm in the Complex. Identification of intermolecular nOe between Bm and ShBle requires complete resonance assignment of Bm when complexed to the protein (Figure 6A). Two Zn(II) complexes of Bm−related derivatives have been assigned in the past under slightly acidic conditions: Zn−bleomycinic acid (*47*) at pH 6.4 and Zn(II)−Bm−A2 (7) at pH 6.7. As our experimental pH (6.5) is very close to these studies, the overall spin system topology is expected to be conserved. The assignments of free Bm were therefore used as a starting point for the assignment of Bm in the Zn−Bm−ShBle complex.

The assignment makes use of ^{1}H-^{1}H correlation spectra recorded in D_2O, where the signals due to the doubly labeled protein are eliminated by isotope filtering. An illustration

A)

^{1}H position	δ ^{1}H (+/-0.05ppm)
A_3-A_4 / P_1-P_2	2.24-2.49 / 3.48 / 2.64-3.64
A5	5.05
P_{12}	2.64
H_6-H_8 / B_5-B_9	8.40 / 8.12
V_1	7.45
V_2	3.65
V_3	3.86
V_4	1.07
V_6/V_7	0.65
T_1	8.04
T_2	3.93
T_4	4.24
T_5	1.48
G_1	5.26
G_2	5.41
G_3	4.03
G_4	3.84
G_5/G_6	3.73
M_1	4.93
M_2	4.18
M_3	4.55
M_4	3.46
M_5	4.08
M_6/$_{6'}$	3.53/ 3.93
R_1	1.78 - 3.24 - 3.51

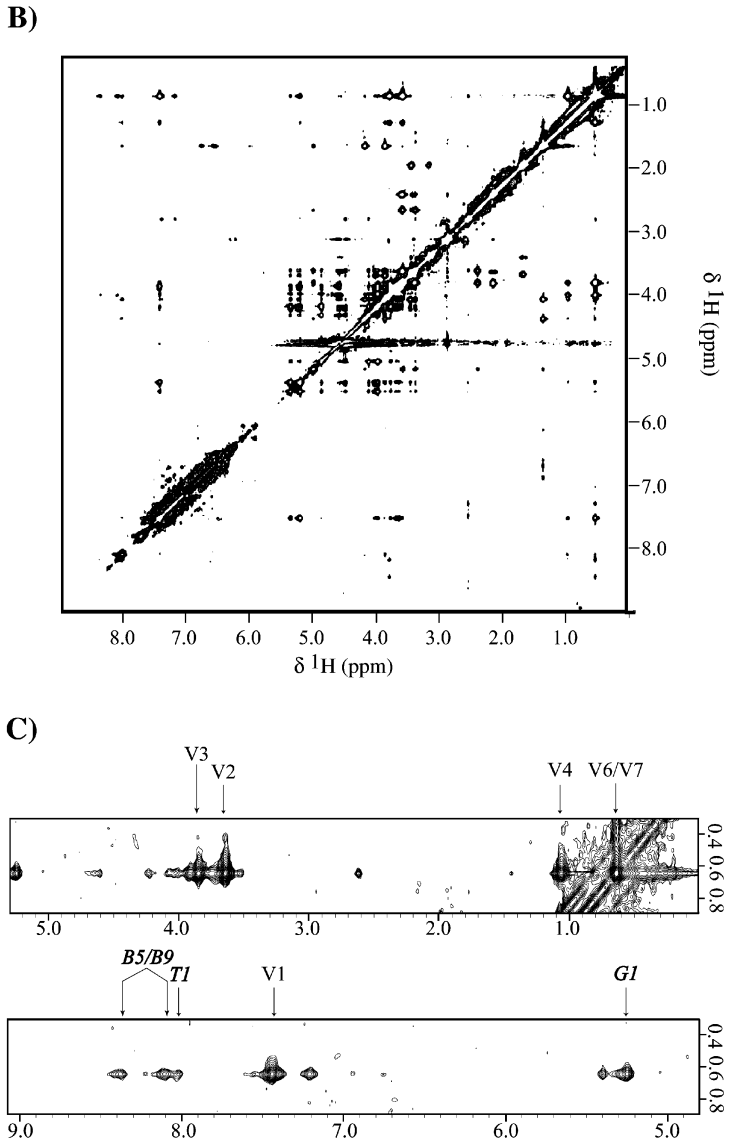

FIGURE 6: Assignment of Bm in the complex. (A) Bm assignment list. Bm atoms are numbered according to Figure 1. Ambiguities are indicated by "/". (B) {^{14}N,^{12}C}-^{1}H-{^{14}N,^{12}C}-^{1}H NOESY spectrum recorded on the Zn−Bm−ShBle complex dissolved in 99% D_2O. (C) Expansion of the spectral region corresponding to nOe correlations between the methyl-valerate groups and other protons.

of a 2D {^{14}N-^{12}C}-^{1}H-{^{14}N-^{12}C}-^{1}H NOESY is given in Figure 6B. The fact that the cross-peaks and diagonal peaks have the same sign shows that the spectrum displays only signals originating from Bm bound to the protein. Three amide protons are still visible in this NOESY spectrum: the amine proton between pyrimidinyl propionamide and β-aminoalanine (A5), and the two amide protons of threonine (T1) and Me−valerate (V1), indicating highly solvent protection from the solvent. The other NH and NH_2 protons are solvent exchanged and not visible in this spectrum. The square pattern in the centre of the NOESY spectrum (between 3.4 and 5.3 ppm) corresponds to the D-manose and L-gulose spin systems. While these two spin systems occupy a narrow spectral region, most of the resonances do no overlap and can be unambiguously assigned. Only the protons labeled in Figure 1 as M6 and M6′ and as G5 and G6 have degenerate resonance frequencies. Whereas the two methyl groups V_6 and V_7 of Me−valerate give rise to non overlapping signals in free Bm, they cannot be distinguished in the complex. The strongest nOe's observed for these two CH_3 are assigned to intraresidue correlations with the V_1, V_2, V_3, and V_4 protons of Me−valerate. The two CH−CH_2 fragments (A3−A4 and P1−P2) were assigned from nOe with the NH (A_5). However it was not possible to discriminate between the two sides. The frequencies of two nOe with the V_2 or V_7 protons were assigned to either the B5/B9 protons of the bithiazole or the H6−H8 of the β-hydroxyhistidine. Distance violations systematically observed during structure calculation when the peaks were assigned to the B5/B9 protons of the bithiazole allowed us to discriminate between the two possibilities.

According to interaction studies of Bm with several metals (Zn, Co, ...), the metal is reported to be generally hexacoordinated. Whereas there is a general agreement for the four planar ligands (amide protons of Ala and of β-hydroxyhistidine and aromatic nitrogens of pyridinylpropionamide and of β-hydroxyhistidine), a number of candidates were proposed for the axial ligands, either from the Bm molecule or from a water molecule. For this study we used the Co(II)−Bm structure recently proposed by Lehmann et al (*42*) as a

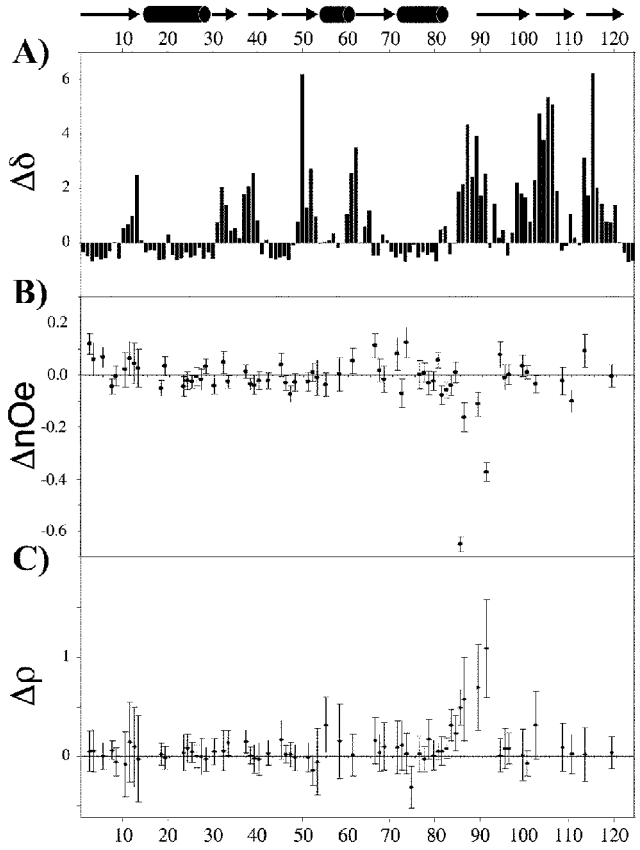

FIGURE 7: Variations of NMR spectral parameters observed upon binding of Zn−Bm to ShBle: (A) chemical shift variations $\Delta\delta$ (see text), (B) steady-state heteronuclear nOe [{^{1}H}-^{15}N nOe (f-ShBle−Zn−Bm−ShBle)] (ΔnOe), and (C) [$R_{1\rho}/\Gamma^{CSA,DD}_{N,NH}$(f-ShBle−Zn−Bm−ShBle)] ($\Delta\rho$). All parameters are displayed as a function of the ShBle sequence.

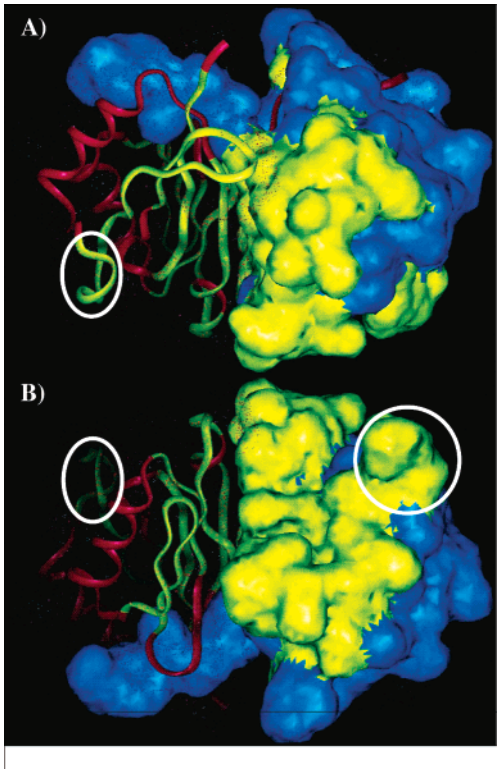

FIGURE 8: Topology of the chemical shift variations on f-ShBle structure. In inset A, the molecule is displayed in the same orientation as in Figure 9, while it is rotated by 180° around an horizontal axis for inset B. This horizontal axis overlaps with one of the diffusion tensor axis (D_z, cf Figure 5). A ribbon representation is used for the left-hand monomeric unit and surface display for the other. Area undergoing significant chemical shift variation upon Zn−bleomycin binding are color coded in yellow for either monomer, while the rest of the protein is shown in red (left-hand unit) and blue (right-hand unit respectively). The loop which becomes less flexible upon Bm binding (according to ^{15}N relaxation data) is highlighted by an ellipse (N85, F86, A89, and G91).

starting point for our computation, where the axial ligands are the primary amine in beta-aminoalanine and the carbamoyl group of the mannose (Figure 1).

Structure Calculation of the Zn−Bm−ShBle Complex. Determination of the Putative Bm Binding Site of ShBle. Some valuable information on the Bm−binding surface of ShBle is easily obtained from NMR chemical shift mapping and deuterium−hydrogen exchange measurements.

The weighted chemical shift variations are reported along the protein sequence in Figure 7A. A total of 69 out of the 124 residues (i.e., 56.5%) exhibit significant chemical shift changes upon Bm binding. These residues can be divided into six amino acids stretches highlighted in yellow in Figure 8: V8−R14, R31−V42, F49−V57, D60−W65, N85−A107, and G113−E121. A first cluster of frequency shifted residues are located at the dimer interface involving both monomeric units, whereas two others involve only a single monomer: residues in the ShBle pocket as well as a groove formed by the side chains of residues Q54, D36, and D37.

Only 6 cross-peaks are visible in the ^{1}H-^{15}N correlation spectrum of f-ShBle recorded 1 month after dissolving the protein in 99% D_2O, whereas the amide protons of 26 residues are still not completely exchanged for the Zn−Bm−ShBle complex. As expected, the six slowly exchangeable amide protons of f-ShBle are all involved in hydrogen bonding according to the X-rays structure of f-ShBle. Except for S_{51}, all slowly exchangeable protons of the free form are also solvent protected in the Zn−Bm−ShBle complex. Twenty-one other amide protons show a sharp reduction of the exchange rate upon Bm binding. Although solvent protection can involve many different mechanisms (*48*), the increasing number of solvent protected amides suggests a more rigid structure of the Zn−Bm−ShBle complex compared to f-ShBle. Most of the residues, which become more solvent-protected after Bm binding, also exhibit significant chemical shift variations upon binding.

The good correlation between these two complementary NMR probes allows us to define a putative binding site of Bm on the f-ShBle structure.

Structural Models from ^{1}H-^{1}H Distance Constraints. Inspection of the NMR restraint list shows that the intermolecular contacts are not at all evenly distributed over the antibiotic. All detected nOe's involve the metal binding site or the V and T fragments of Bm. It should be noted that the sensitivity of the experiment only allowed detection of interproton contacts involving at least one methyl group. No nOe was detected between the protein and the variable part (R_1) of Bm. In addition, no structural information for the bithiazole tail was available due to the lack of resonance assignment for this part of Bm. The set of intramolecular Bm constraints can be classified in two categories: (1) nOe interactions inside the metal binding site, confirming the fold

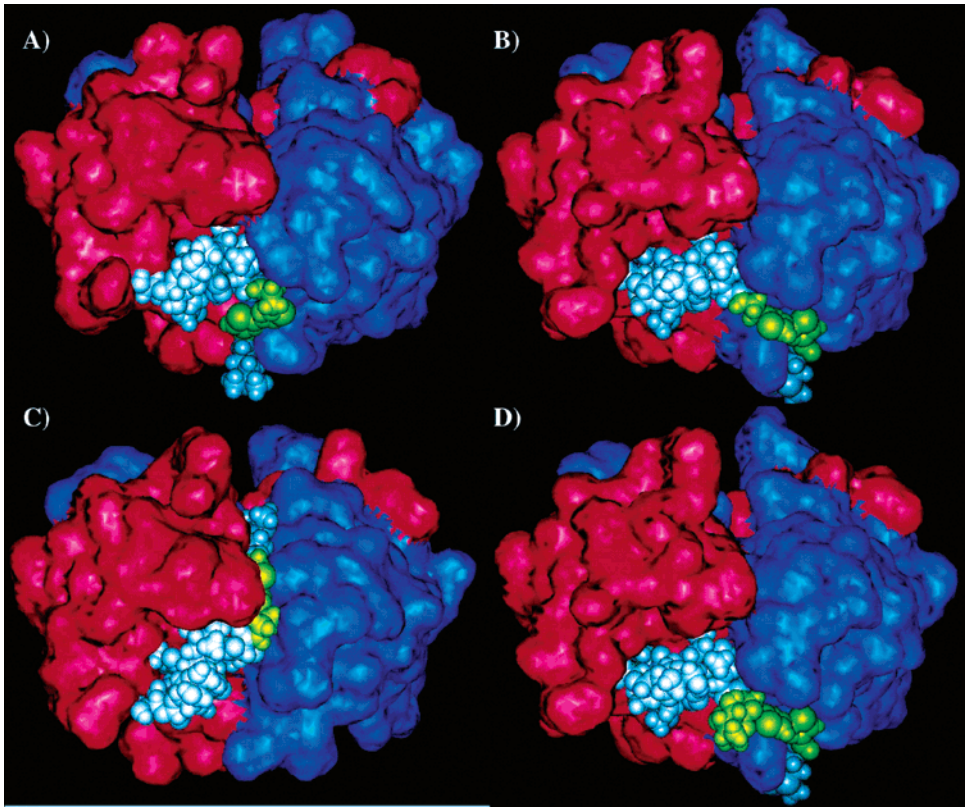

FIGURE 9: Model structure: (A) F_1, (B), F_2, (C) F_3, and (D) F_4. The two monomers surfaces are displayed in red and blue. The Bm related molecule is figured in CPK mode, and the bithizole part is colored in yellow.

around the metal, and (2) constraints between the V and the carbohydrates part of T and A, which define the orientation of the arm with respect to the metal-binding site.

The average experimental target function for set **S**[1] (31 structures) is 1.69 kcal mol^{-1} with a standard deviation, with respect to the mean, of 0.50 kcal mol^{-1}. The best structure exhibits an experimental target function close to 0.7 kcal mol^{-1}. We have analyzed these structures with respect to two parts of the Bm molecule: the metal binding site and the bithiazole tail. If we focus on the relative orientation and position of the metal binding site with respect to the protein, a major group (14 structures) emerges with a rather well conserved conformation. The remaining structures (17 structures), which show much greater heterogeneity associated with a slightly higher experimental energy, differ from the main group by slight reorientation of the metal binding site in the pocket. On the basis of the experimental target function, we will restrict our discussion to the major group of structures.

Whereas the conformation of the metal binding site is well preserved in these 14 structures (rmsd < 0.5 Å), two families F_1 and F_2 can be identified for the conformation of the bithiazole tail. In the F_1 family, the two bithiazole cycles are folded back toward the metal binding site and the bithiazole moiety is located on the left-hand side of Q54. In the F_2 family, the two thiazole cycles are far away from the metal binding site and are inserted in the above-mentioned groove. The two structures with the lowest distance violation for each of the two families are shown in Figure 9A,B and will be discussed with respect to the structure of f-ShBle (*15*) and the recently published X-rays structures of the Bm−BLMT (*17*) and Co(II)−Bm−BLMA (*21*) (PDB entries 1ECS and 1EWJ, respectively). The metal binding site exhibits the same conformation as that found in the two crystal structures—i.e., the gulose is facing the protein flexible loop—but a 180° rotation along the axial metal ligandsaxis is needed to superimpose our orientation on the Bm−ShBle model. The conformation of the bithiazole tail in both NMR families of structures (F_1 and F_2) differs from the two crystal structures where the arm is buried in a crevice at the dimer interface, apparently stabilized by hydrophobic interactions between aromatic side chains of the protein and the bithiazole rings of Bm. A similar conformation has also been proposed for the Bm−ShBle model. In the NMR structures, the bithiazole tail conformation is not determined by experimental distance restraints, but only by the primitive force field of the molecular dynamics calculation. The absence of experimental constraints between the bithiazole tail and the protein may be due to missing assignments for the bithiazole protons and the limited sensitivity of the isotope filtered NOESY experiments. We cannot exclude that the bithiazole tail is in a conformation similar to the one found in the previous X-rays studies but that this conformation is not found in the limited conformational ensemble, due to steric hindrance from side-chains in the dimer interface. To evaluate if the insertion of the bithiazole rings in the crevice at the dimer interface is compatible with our NMR data, we have added some distances between the bithiazole rings and the protein derived from the Sh−Ble model to our experimental constraint list (set **S**[2]). Despite the added distances the residual distance violation for the 13 structures (family F_3) is still small (lowest-energy conformer = 4.5 kcal mol^{-1}) (Figure 9).

In summary, three structural models were computed using two different distance restraint sets. While the conformation of the bithiazole arm differs among these structures, the metal

binding site appears well defined. The metal-binding part of Bm is in contact with a single monomeric unit of ShBle and interacts with a concave area that is already carved out in the free protein. In all three structures, a substantial surface (between 47% and 53%) is involved in the protein−ligand interaction. ^{15}N relaxation data recorded for the free ShBle protein and the Zn−Bm−ShBle complex show that the molecular tumbling is not significantly affected by the binding of the antibiotic, which increases the overall molecular weight by nearly 10%. This finding is in agreement with the insertion of the Bm metal-binding part inside a pocket of ShBle.

Variation in Local Dynamics due to Bm Binding. ^{15}N relaxation measurements were carried out on f-ShBle and Zn−Bm−ShBle to assess the changes in internal mobility upon binding. Panels B and C of Figure 7 show, respectively, the variation of the {^{1}H}-^{15}N nOe between f-ShBle and Zn−Bm−ShBle ($nOe^{free} - nOe^{bound}$)) and the variation of the relaxation rate ratio ρ ($\rho^{free} - \rho^{bound}$). This comparison is restricted to residues with resolved ^{1}H-^{15}N correlation peaks for both, the free and the Bm−bound state (Figure 2, Supporting Information). Only four residues exhibit a significant variation of these two experimental probes upon Bm binding. These four residues are located between helix-α_3 and the β_6 strand. This region is not well structured in the X-rays structure of f-ShBle (Figure 8), where all residues between Ser 83 and Gly 91 exhibit higher than average B-factors (*15*). The *B*-factors of their C^α carbons are all above 40 Å^2 (with a maximum around residues 87−88), whereas the average over the entire molecule is close to 25 Å^2. The structural disorder in this region of the molecule is also confirmed by the NMR conformational probes, ^{1}H-^{1}H nOe and CSI (Figure 3A,B). The reported variations of {^{1}H}-^{15}N nOe and ρ values clearly demonstrate that this loop, inherently flexible in the free molecule, becomes more rigid upon binding on both monitored time scales (picosecond−nanosecond and microsecond−millisecond). The same behavior is also observed in the Bm−BLMT structure, where the *B*-factors of this loop are lower than in the free form (*17*). Note that the amide proton of residue W_{78} in the second turn of the helix-α_3 (three turns) exhibits slow rate exchange. The rigidity of the following loop may thus contribute to stabilize the helix.

DISCUSSION

The specific interaction between ShBle and Me−Bm has been confirmed by our NMR study using several experimental probes. The metal-binding domain of Bm interacts with a concave area observed on the surface of the free protein. The key role of this concavity has previously been proposed by modeling based on the X-rays structure of f-ShBle (*15*) and more recently confirmed by two very recent studies on similar systems, Bm−BLMT (*17*) and the Co(II)−Bm−BLMA (*21*). In addition, we have shown that two other regions of the protein (the dimer interface and the groove between Q54 and D36−D37) exhibit significant chemical shift variations on binding. Whereas these variations provide evidence that these two regions are involved in the interaction, this result requires further confirmation.

NMR data from Zn−Bm−ShBle provide clear evidence that the conformation of the protein in the complex does not dramatically change from the free protein observed by crystallography (*15*). The variation of the HSQC spectrum upon titration of Bm corresponds to slow exchange and the detection of a single set of peaks for the bound protein is in favor of a homogeneous population. This last point is confirmed by the detection of slow exchangeable protons for Bm in the Bm−ShBle complex, protons which have never been observed in the Zn−Bm free form (*7*).

Three families of structures were obtained, two based only on NMR data (F_1 and F_2) and another by combination of NMR data and distance constraints derived from previous Bm−ShBle modeling (F_3). While the metal-binding site of Bm is conserved, substantial differences among these three families are observed for the location of the Bm arm, as no nOe was detected between the bithiazole arm and the protein. We can conclude that the previously proposed metal-binding site interacts with the protein in a similar way to that reported for Bm−BLMT (*17*) and the Co(II)−Bm−BLMA (*21*) that the conformation of the bithiazole arm can adopt the predicted conformation without seriously violating our measured distances.

Earlier NMR studies of Co(II)−Bm (*42*) have shown that the presence of a metal ion induces the folding of not only the metal binding site of Bm but also of the bithiazole-tail moiety, whereas the free form remains totally unstructured. While the lack of any preexisting fold (in the absence of metal) may promote the insertion in the dimer crevice, an alternative multistep mechanism can also be proposed: the Zn−Bm complex first interacts with the protein as a folded state (as shown in F_1 and F_2 NMR models); then the bithiazole-tail moiety unfolds when interacting with the protein and ultimately inserts in the crevice with a 30° rotation of the metal-binding site. Such a scenario is in agreement with the need of preincubating the Bm−BRP solution before initiating the crystal growth.

The three families of structures should also be analyzed in the broad context of antibiotic resistance for Bm analogues such as phleomycin and tallysomycin (*14*). It has been reported that these molecules can also bind to BLMT and ShBle (*12*, *51*) and thus carry antibiotic resistance. Their chemical structures are reported in Supporting Information Figure 3. Phleomycin (Plm) and Bm differ only at the level in the first bithiazole ring, where B5−B6 is single bond for Plm instead of a double in Bm. In the case of tallysomycin (Tlm), two protons at position B2 and B3 are respectively replaced by a 4-amino-4,6-deoxy-L-idose and a hydroxyl group. As the metal binding domain of Tlm is chemically identical to that of Bm (*49*), one can reasonably postulate that it should interact with the proteins in a rather similar way. In contrast, the presence of a bulky group instead of a single proton at position B2 may alter the interaction of this fragment with the proteins. When the monosaccharide is manually added to the F_3 conformer, a steric clash occurs with P101. In contrast, one can easily anchor the same bulky group on any member of the F_2 family and accommodate it without any need for reorientation or steric hindrance. This is illustrated on Figure 9D, where a 4-amino-4,6-deoxy-L-idose has been added to the Bm molecule starting from the conformation pictured in Figure 9B.

In conclusion, we have shown that our NMR data are in general agreement with the model proposed by Dumas et al (*15*) on the basis of the X-rays structure of the free ShBle,

although the orientation of the metal binding site with respect to the protein surface is different based on our data. Two conformations with similar positions of the metal binding site have been determined, and the bithiazole tail has been located in a groove between Q54 and D36−D37. The previously proposed conformation with the bithiazole tail in the dimer interface is however also in agreement with our measured data. Heteronuclear relaxation measurements identify differential dynamics in the loop between Ser 83 and Gly 91, which is inherently flexible in the free molecule and becomes more rigid upon binding on both the ps-ns and μs-ms time scales.

ACKNOWLEDGMENT

This work was supported by the C.E.A., the C.N.R.S. (France), and MSI Technologies (San Diego). We thank F. Halgand for performing all mass-spectrometry measurements.

SUPPORTING INFORMATION AVAILABLE

Figure 1: Chemical structure of phleomycin and tallysomycin. Figure 2: List of residues used as input for the diffusion tensor calculation. Figure 3: Consensus set of data used in the dynamic study. As the pattern of overlapping peaks is different in the ^{1}H-^{15}N HSQC of f-ShBle ans Zn−Bm−ShBle, only peaks which do not overlap in both spectrum are taken into account for this analysis. Table 1: Intermolecular NOESY interactions between ShBle and Bm. Bm and ShBle position are numbering as in Figures 1 and 3, respectively. For Bm, A is for A_3 and A_4, and P for P_1 and P_2. A "/" notifies an ambiguity. Table 2: Observed intramolecular NOESY interactions inside the Bm molecule. Bm numbering according to the definition given in Figure 1. "−" indicates an interaction between two nuclei, while ambiguously assigned nuclei are separated by a slash (/). Table 3. Additional nonexperimental distances between the bithiazole fragment and ShBle obtained from the modeled Bm−ShBle complex (PDB entry 1BYL). These distances were part of the $\mathbf{S^2}$ data set used to check the compatibility of the experimental NMR data with the previously proposed model. This material is available free of charge via the Internet at http://pubs.acs.org.

REFERENCES

1. Umezawa, H., Maeda, K., Takeuchi, T., and Okami, Y. (1966) *J. Antibiot.* (*Tokyo*), *19*, 200−209.
2. Umezawa, H. (1971) *Pure Appl. Chem. 28*, 665−680.
3. Blum, R. H., Carter, S. K., and Agre, K. (1973) *Cancer 31*, 903−14.
4. Sausville, E. A., Peisach, J., and Horwitz, S. B. (1976) *Biochem. Biophys. Res. Commun. 73*, 814−822.
5. Burger, R. M., Projan, S. J., Horwitz, S. B., and Peisach, J. (1986) *J. Biol. Chem. 261*, 15955−15929.
6. Nunn, A. D. (1976) *Jpn. J. Antibiot. 29*, 1102−1108.
7. Akkerman, M. A., Haasnoot, C. A., and Hilbers, C. W. (1988) *Eur. J. Biochem. 173*, 211−25.
8. Otvos, J. D., Antholine, W. E., Wehrli, S., and Petering, D. H., (1996) *Biochemistry 35*, 1458−1465.
9. Konishi, M., Saito, K., Numata, K., Tsuno, T., and Asama, K., (1977) *J. Antibiot.* (*Tokyo*) *30*, 789−805.
10. Sugiyama, M., Kumagai, T., Shionoya, M., Kimura, E., and Davies, J. E., (1994) *FEMS Microbiol. Lett. 121*, 81−85.
11. Sebti, S. M., DeLeon, J. C., and Lazo, J. S. (1987) *Biochemistry 26*, 4213−4219.
12. Drocourt, D., Calmels, T., Reynes, J. P., Baron, M., and Tiraby, G. (1990) *Nucleic Acids Res. 18*, 4009−4012
13. Suzuki, M., Thompson, C. J., Kumagai, T., Suzuki, K., Deblaere, R., Villarroel, R. and Davies, J. (1994) *Gene 151*, 11−16.
14. Collis, C. M., and Hall, R. M. (1984) *Plasmid 14*, 143−151.
15. Dumas, P., Bergdoll, M., Cagnon, C.; Masson J.-M. (1994) *EMBO J. 13*, 2483−2492.
16. Kawano, Y., Kumagai, T., Muta, K., Matoba, Y., Davies, J., and Sugiyama, M. (2000) *J. Mol. Biol. 295*, 915−925.
17. Maruyama, M., Kumagai, T., Matoba, Y., Hayashida, M., Fujii, T., Hata, Y., and Sugiyama, M., (2001) *J. Biol. Chem. 276*, 9992−9999.
18. Semon, D., Movva, N. R., Smith, T. F., el Alama, M., and Davies, J. (1987) *Plasmid 17*, 46−53.
19. Gatignol, A., Durand, H., and Tiraby, G. (1988) *FEBS Lett. 230*, 171−175.
20. Sheldon, P. J., Mao, Y., He, M., and Sherman, D. H. (1999) *J. Bacteriol. 181*, 2507−2512.
21. Sugiyama, M., Kumagai, T., Hayashida, M., Maruyama, M., and Matoba, Y. (2002) *J. Biol. Chem. 277*, 2311−2320.
22. Weinbach, J., Camus, A., Barra, J., Dumont, P., Julian, M., Cros, S., Babinet, C., Tiraby, G. (1996) *Cancer Res. 56*, 5659−65.
23. Tran, P. L., Weinbach, J., Opolon, P., Linares-Cruz, G., Reynes, J. P., Gregoire, A., Kremer, E., Durand, H., and Perricaudet, M. (1997) *J. Clin. Invest. 99*, 608−17.
24. Vanbelle, C., Muhle-Goll,C., Rémy, M.-H., Masson, J.-M., Marion, D., and Brutscher, B. (2000) *J. Biomol. NMR 18*, 177−178.
25. Sambroock, J., Fritsch, E. F., and Maniatis, T. (1989) *Molecular Cloning: A Laboratory Manual*, 2nd ed., Cold Spring Harbor Laboratory Press, Plainview, NY.
26. Takita, T., Muraoka, Y., Nakatani, T., Fujii, A., Umezawa, Y., and Naganawa, H. (1978) *J. Antibiot.* (*Tokyo*) *31*, 801−804.
27. Farrow, N. A., Muhandiram, R., Singer, A. U., Pascal, S. M., Kay, C. M., Gish, G., Shoelson, S. E., Pawson, T., Forman-Kay, J. D. and Kay, L. E. (1994) *Biochemistry 33*, 5984−6003.
28. Cordier, F., Caffrey, M., Brutscher, B., Cusanovich, M. A., Marion, D., Blackledge, M. (1998) *J. Mol. Biol. 281*, 341−361.
29. Brutscher, B., Bruschweiller, R., and Ernst, R. R. (1997) *Biochemistry 36*, 13043−13053.
30. Pervushin, K., Riek, R., Wider, G., and Wüthrich, K. (1997) *Proc. Natl. Acad. Sci. U.S.A. 94*, 12366−12371.
31. Cordier, F., Dingley, A. J., and Grzesiek, S. (1999) *J. Biomol. NMR 13*, 175−180.
32. Wang, A. C., and Bax, A. (1993) *J. Biomol. NMR, 3*, 715−720.
33. Lipari, G., and Szabo. A. (1982) *J. Am. Chem. Soc. 104*, 4546−4559 and *J. Am. Chem. Soc. 104*, 4559−4570.
34. Woessner, D. E. (1962) *J. Chem. Phys. 37*, 647−660.
35. Dosset, P., Hus, J.-C., Blackledge, M. J., and Marion, D. (2000) *J. Biomol. NMR 16*, 23−28.
36. McCallum, S. A., Hitchens, T. K., Torborg, C., and Rule, G. S. (2000) *Biochemistry 39*, 7343−7356.
37. Gemmecker, G., Olejniczak, E. T., and Fesik, S. W. (1992) *J. Magn. Reson. 96*, 199−204.
38. Sklenár, V., Piotto, M., Leppik, R., and Saudek, V. (1993) *J. Magn. Reson. 102*, 241−245.
39. Leupin, W., Otting, G., Amacker, H., and Wüthrich, K. (1990) *FEBS Lett. 263*, 313−316.
40. van Nuland, N. A., Kroon, G. J., Dijkstra, K., Wolters, G. K., Scheek, R. M. and Robillard, G. T. (1993) *FEBS Lett. 315*, 11−15.
41. McKay, R. T., Pearlstone, J. R., Corson, D. C., Gagne, S. M., Smillie, L. B., and Sykes, B. D. (1998) *Biochemistry 37*, 12419.
42. Lehmann, T. E., Serrano, M. L., and Que, L. Jr. (2000) *Biochemistry 39*, 3886−3898.
43. Nicholls, A., Sharp, K., and Honig, B. (1991) *Proteins 11*, 281−296.
44. Lehmann, T. E., Ming, L. J., Rosen, M. E., and Que, L., Jr. (1997) *Biochemistry, 36*, 2807−2816.
45. Wüthrich, K. (1986) *NMR of Proteins and Nucleic Acids*, pp 162−175, Wiley-Interscience, New York.
46. Wishart, D. S., and Sykes, B. D. (1994) *J. Biomol. NMR 4*, 171−180.
47. Oppenheimer, N. J., Rodriguez, L. O., and Hecht, S. M. (1979) *Biochemistry 18*, 3439−3445.
48. Milne, J. S., Mayne, L., Roder, H., Wand, A. J., and Englander, S. W. (1998) *Protein Sci. 7*, 739−745.
49. Dabrowiak, J. C., Greenway, F. T., Santillo, F. S., and Crooke, S. T., (1979) *Biochem. Biophys. Res. Commun. 91*, 721−729.
50. Halgand, F., personal communication.
51. Drocourt, D., personal communication.

BI0267341